Noname manuscript No.
(will be inserted by the editor)

Linear instability in the wake of an elliptic wing

Wei He · Juan Ángel Tendero · Pedro Paredes · Vassilis Theofilis

Received: 2 March 2016 / Accepted: 14 June 2016

Abstract Linear global instability analysis has been performed in the wake of a low aspect ratio three-dimensional wing of elliptic cross-section, constructed with appropriately scaled Eppler E387 airfoils. The flow field over the airfoil and in its wake has been computed by full three-dimensional direct numerical simulation at a chord Reynolds number of $Re_c = 1750$ and two angles of attack, $AoA = 0^\circ$ and 5°. Point vortex methods have been employed to predict the inviscid counterpart of this flow. The spatial BiGlobal eigenvalue problem governing linear small-amplitude perturbations superposed upon the viscous three-dimensional wake has been solved at several axial locations and results were used to initialize linear PSE-3D analyses without any simplifying assumptions regarding the form of the trailing vortex system, other than weak dependence of all flow quantities on the axial spatial direction. Two classes of linearly unstable perturbations were identified, namely stronger-amplified symmetric modes and weaker-amplified antisymmetric disturbances, both peaking at the vortex sheet which connects the trailing vortices. The amplitude functions of both classes of modes were documented and their characteristics were compared with those delivered by local linear stability analysis in the wake near the symmetry plane and in the vicinity of the vortex core. While all linear instability analysis approaches employed have delivered qualitatively consistent predictions, only PSE-3D is free from assumptions regarding the underlying

W. He
School of Aeronautics, Universidad Politécnica de Madrid, Pza. Cardenal Cisneros 3, E-28040 Madrid, SPAIN
Tel.: +34-91-3363298
Fax: +34-91-3363295
E-mail: w.he@alumnos.upm.es

J. A. Tendero & P. Paredes
School of Aeronautics, Universidad Politécnica de Madrid, Pza. Cardenal Cisneros 3, E-28040 Madrid, SPAIN

V. Theofilis
Center for Engineering Dynamics, University of Liverpool, Browlow Hill, Liverpool L69 3GH, UK

Theoretical and Applied Mechanics Laboratory, Department of Mechanical Engineering, Universidade Federal Fluminense, Rua Passo da Patria 156, Niterói, RJ 24210-240, BRAZIL

base flow, and should thus be employed to obtain quantitative information on amplification rates and amplitude functions in this class of configurations.

Keywords Elliptic wing · Trailing vortex system · Global linear instability

1 Introduction

Instability analysis of vortical flows has been at the center of Fluid Mechanics interests for decades, both from a fundamental and from an applied research point of view. Traditionally, two different paths are followed in the analysis. The first approach, collectively referred to as *point-vortex* methods, dates back to the classic works of Von Kármán [29,30] and is based on the study of small-amplitude deviations of vortices from their undisturbed equilibrium position [2,32]. Crow [12] and Jiménez [28] introduced this approach to the inviscid analysis of instability in the counter- and co-rotating pairs of vortices, respectively. Crouch [11] extended this methodology to address modal and non-modal linear instability of a four-vortex system and showed that transient growth is the dominant linear instability mechanism for this class of flows; results were later confirmed by Fabre and Jacquin [15] and others. In the second approach the viscous equations of motion are linearized about a nominally steady laminar base flow and the linear eigenvalue problem is solved either by neglecting viscosity [34] or at a given finite value of the flow Reynolds number [33,40]. The limited number of exact solutions of the equations of motion corresponding to viscous vortices led the majority of the analyses available in the literature to monitor idealized vortex solutions, such as the classic Batchelor model [3] and its simplifications, or various models of isolated vortices [27]. In most analyses no axial flow is considered and, in addition, viscous diffusion of the vortex along the axial direction is neglected.

The discovery of long [12] and short-wavelength instabilities [53,35] in systems of counter-rotating vortices and the association of these mechanisms with those observed in the trailing-vortex system of commercial transport aircraft in cruise provided a boost to efforts aiming at the destruction of the coherence of trailing vortex systems based on identification and exploitation of physics-based linear instability mechanisms. Linear global instability analysis of a counter-rotating viscous pair of vortices commenced with the work of Hein & Theofilis [23], who recovered the eigenmodes of a vortex system initialized using the so-called $q-$vortex simplification of the Batchelor vortex model. This work demonstrated that knowledge gained from instability analysis of isolated viscous vortices [40,19] may be of limited use for the description of instability of vortical systems, except in the limit of the separation between the cores of the counter-rotating vortices becoming very large in terms of the wing span. The subsequent work of Jacquin *et al.* [27] showed that vortex-core instabilities pertinent to either of the inner or the outer pair of a four-vortex system may be recovered as distinct eigenmodes in BiGlobal linear instability analysis considering the entire vortex system as its base flow. González *et al.* [20] demonstrated that elliptic instability of a pair of counter-rotating viscous vortices with axial flow may be analyzed using BiGlobal linear analysis. The eigenfunctions obtained bore no resemblance to those pertinent to analysis of isolated vortices based on classic local linear theory [19], thus making global analysis the method of choice to address linear instability of systems of viscous vortices in close proximity.

Theoretical efforts to analyze the instability of models of closely-spaced viscous vortices continued with the work of Meunier & Leweke [41] on a co-rotating vortex pair, and that of Lacaze *et al.* [31] who employed direct numerical simulation to study instability of a Batchelor vortex subject to the far-field strain of a second vortex, the latter not explicitly considered in the analysis. Duck [14] solved the BiGlobal analogue of the Rayleigh equation pertinent to systems of two or four counter-rotating vortices and went on to describe their breakdown process. Interestingly, at conditions at which the base flows considered in the viscous analysis of Lacaze *et al.* [31] and the inviscid work of Duck [14] were closely related, the instability results of the two works were also qualitatively analogous, despite the large disparity in magnitude of axial flow considered in the respective works. In a similar spirit, Brion *et al.* [6], Tendero *et al.* [49,50] and Benton & Bons [4] have demonstrated that point-vortex and viscous BiGlobal instability analyses of a pair of axially-homogeneous counter-rotating vortices deliver equivalent results, provided the Reynolds number and the spacing of the vortices are taken to be sufficiently high.

Global linear theory [52] has now advanced sufficiently in order to address instability in the wake of a three-dimensional wing without the need to resort to the severe approximations of classic (local) analysis. The assumption of homogeneity along the azimuthal spatial direction, which underpins local linear theory applied to analyze instability of isolated vortices, is no longer needed (or indeed appropriate) when dealing with a system of vortices emanating from a finite low aspect-ratio wing. Instead, BiGlobal linear theory can be used to fully resolve any distribution of vorticity on a given plane Oyz normal to the axial spatial direction, x, considering the latter direction as homogeneous. Application of viscous BiGlobal linear modal analysis to an isolated $q-$vortex [8,20,46] has been shown to deliver identical results with those of the local analysis [40]; this point is further addressed in what follows.

Applying global linear theory to the system of multiple vortices formed in the near-wake behind a real wing, a number of flow properties inaccessible to classic analysis based on inviscid methods for the computation of the base flow or linear stability analyses of one-dimensional profiles can be taken into account. First, the interaction of trailing vortices due to their proximity introduces a downwash velocity which needs to be taken into account. This was first accomplished by Tendero *et al.* [49], who showed that the eigenvalue spectrum obtained by BiGlobal analysis of a pair of descending counter-rotating vortices is displaced compared to that delivered by analysis of a frozen base flow. Viscous diffusion along the axial direction is also relevant for the base flow definition at all but the highest Reynolds numbers; this flow property was introduced in the analysis of an isolated non-parallel Batchelor vortex by Heaton *et al.*[22]. Of course, any global linear instability analysis of vortex systems behind realistic wings should also account for a non-negligible amount of axial velocity component, related with the flight velocity, as well as with flow turbulence.

The present work revisits the issue of linear global instability of a system of counter-rotating vortices by addressing, for the first time, instability of the entire trailing vortex system behind a three-dimensional finite aspect-ratio wing of elliptical planform, placed at zero- and a small finite angle of attack to the oncoming flow. The wing considered is based on the Eppler-387 airfoil and has an elliptical planform defined in the recent experiments of Xue *et al.* [54]. This

airfoil was chosen on account of the absence of laminar separation at low Reynolds numbers and low angles of attack, an assumption which has only been verified in the $AoA = 0^\circ$ basic flow results obtained herein. The full roll-up process in the near-wake as well as the formation of the trailing vortex system are described by three-dimensional direct numerical simulation. In addition, point-vortex methods have been used to predict the evolution of the inviscid counterpart of the flow field obtained in the DNS, compare integral flow quantities obtained by either the viscous or the inviscid analysis at the same parameters and predict the long-time behavior of the inviscid flow in an efficient manner.

Subsequently, instability of the trailing vortex system is analyzed by solving the spatial BiGlobal linear viscous eigenvalue problem [13] at selected locations along the axial direction, to unravel the response of the steady laminar flow to small-amplitude convectively unstable perturbations of constant frequency introduced into the flow. Finally, the axial viscous diffusion and downwash of the base flow are simultaneously taken into account by a linear PSE-3D [1] analysis of the entire trailing-vortex system. The PSE-3D analysis is the three-dimensional extension of the parabolized stability equations [10,46,13] and is initialized at a given axial location by solution of the spatial BiGlobal eigenvalue problem. This provides a first approximation of the streamwise wavenumber of the linear perturbations; once converged, the linearized PSE-3D equations are marched along the axial spatial direction and the results obtained are compared with those previously delivered by solution of the spatial BiGlobal eigenvalue problem in an attempt to quantify the differences in flow stability characteristics predicted by the respective approaches.

An alternative experimental work on which the present analysis could have focused is that by Higuchi *et al.*[26]. These authors have provided a wealth of information on flow development on a elliptic wing of aspect ratio 3 constructed on the basis of the NACA $66_2 - 415$ chord section. However, interpretation of those results suggests that several linear instability mechanisms are active at the Reynolds number $Re \approx 5 \times 10^4$ at which that experiment was performed, related to flow separation on the wing and the subsequent roll-up of the vortex sheet into laminar transitional or turbulent vortices. Consequently, it was decided to first perform analyses at the low Reynolds numbers at which the Xue *et al.*[54] experiments are performed, identify the linear perturbations that lead steady laminar flow to unsteadiness and systematically advance to instability analyses at higher Reynolds numbers at a later stage.

Section 2 presents the theoretical background used in the present analysis, starting with the problem definition in 2.1, followed in section 2.2 by a brief introduction of the direct numerical simulation work employed to compute the base state analyzed and the point vortex method used to predict the inviscid evolution of this flow. A discussion follows of the global instability analysis concepts employed, spatial BiGlobal linear modal analysis in 2.4 and the PSE-3D concept in 2.5. Results of these global instability analysis methodologies are presented in section 3 and are compared with results obtained by classic linear stability theory at appropriate portions of the wake. Concluding remarks are presented in section 4.

[1] also known as *plane-marching PSE[1]*

2 Theory

2.1 Problem definition

An orthonormal Cartesian frame of reference is considered, in which x denotes the axial spatial direction, while y and z are the normal and spanwise spatial directions, respectively. A three-dimensional wing model is constructed based on the low-Reynolds number Eppler E-387 airfoil. The wing planform is elliptical, its major axis being the wing span, $b = 1.714$, while its minor axis is the chord $c = 1$ of the E-387 airfoil at the plane of symmetry, $z = 0$; a low aspect ratio AR=1.7 wing is thus obtained. The airfoils defined by cuts of the wing by planes normal to the Oz axis at locations $0 \leq z \leq b/2$ are also E-387 profiles, the respective chords of which are scaled such that they fit the elliptical planform at each z location; an image is shown in the left part of Figure 1.

Direct numerical simulations for the calculation of the basic state were performed using the nek5000 open source code [16]. The software *Gambit* was used to construct the three-dimensional meshes in which the (half-) wing model has been embedded, as shown in the right part of Figure 1. Within each of the macro-elements shown a high order polynomial was chosen in the spectral element code, until convergence was reached, as will be discussed shortly.

An alternative approach for the generation of a fully consistent base flow which respects all of the flow properties of a trailing-vortex system has been discussed by Paredes *et al.* [45], who solve the Parabolized Navier Stokes equations in order to compute both viscous diffusion and downwash of a counter-rotating vortex system. This approach has not been followed in the present analysis. Instead, classic point-vortex [32] computations, initialized using the vorticity distribution extracted from the DNS results immediately downstream of the wing, have been performed in order to obtain a rapid estimate regarding the evolution of the wake behind the wing in the inviscid flow limit.

The instability analysis consists of first using the DNS to compute a steady laminar viscous basic flow solution of the incompressible Navier-Stokes and continuity equations around the three-dimensional wing, denoted as $\bar{\mathbf{q}} = (\bar{u}, \bar{v}, \bar{w}, \bar{p})^T$. It contains the basic flow velocity components and associated pressure, all of which are *inhomogeneous functions of all three spatial coordinates*. Subsequently, small-amplitude three-dimensional unsteady perturbations, denoted by $\tilde{\mathbf{q}}(x, y, z, t) = (\tilde{u}, \tilde{v}, \tilde{w}, \tilde{p})^T$, are introduced into the full equations of motion and the latter are linearized around the basic state, leading to the three-dimensional Linearized Navier Stokes equations (LNSE) that need to be solved in order to obtain the linear instability characteristics of the flow in question.

Three sets of assumptions on the form of linear perturbations $\tilde{\mathbf{q}}$ are made in the present work. First, the DNS-obtained base flow is post-processed to extract one-dimensional velocity profiles amenable to local linear instability analysis. The inherent parallel flow assumption restricts the locations in the wake at which local analysis may be performed in a meaningful way to either the wake at large distances from the trailing vortices, or the immediate vicinity of the vortex cores. At these locations the spatial Orr-Sommerfeld equation and its axisymmetric analog will be solved in order to recover the characteristics of the unstable linear local perturbation, $\tilde{\mathbf{q}}_0$.

The second set of assumptions leads to a class of perturbations, $\tilde{\mathbf{q}}_1$, that comprise periodic disturbances along the axial spatial direction, implying that the $x-$derivatives of the basic state are neglected in the instability analysis. In addition, the perturbations are taken to be harmonic in time. The resulting theoretical framework employed is based on the spatial linear BiGlobal modal concept [52] and will be briefly discussed in what follows. It is clear that the assumption of axial homogeneity, invariably made in the vast majority of instability analyses of isolated vortices and literally all presently available literature dealing with linear instability analysis of systems of vortices in the wake of a wing, can only be justified at some distance downstream of the wing, in the so-called near mid-field of the wake [27]. In what follows, spatial BiGlobal analysis will be performed at a number of axial locations in the near mid-field in a range of (low) Reynolds numbers.

The third class of perturbations analyzed, $\tilde{\mathbf{q}}_2$, will retain the harmonic assumption in time but relax homogeneity of the base flow along the axial spatial direction in order to permit viscous vortex diffusion along x. This is accomplished by incorporating first derivatives of the base flow along this direction into the linear instability analysis framework. Short of resorting to full-scale direct numerical simulation, the form of linear (and non-linear) perturbations $\tilde{\mathbf{q}}_2$ that is consistent with this assumption is that described by the PSE-3D concept [52]. Unlike the eigenvalue problem solution of the spatial BiGlobal approach, PSE-3D is based on space-marching of the appropriate LNSE on the Oyz plane along the axial spatial direction. The plane marching is initialized using results of the spatial BiGlobal approach at a given axial location and it is interesting to compare the instability results obtained by the space marching of the PSE-3D with those delivered by the spatial BiGlobal analyses at selected axial locations. In this manner, the appropriate linear instability analysis model for this class of flows can be established.

2.2 Base state computation

2.2.1 Direct numerical simulations

Incompressible fluid flow is considered in the present work, taking the kinematic viscosity, ν, as a free parameter. In this manner, two Reynolds numbers could be defined, that based on mid-plane chord, Re_c, and the more commonly used in instability analysis of vortex systems, Reynolds number based on circulation, Re, respectively defined as

$$Re_c = \frac{U_\infty c}{\nu}, \qquad \text{and} \qquad Re = \frac{\Gamma}{\nu}. \tag{1}$$

The converged results of the simulations were post-processed in order to define the flow circulation at an axial location x_i at which the analysis was performed, using

$$\Gamma = \int\int \zeta(x_i, y, z) dy dz, \tag{2}$$

where $\zeta = -\partial_y \bar{w} + \partial_z \bar{v}$ is the axial vorticity component at x_i.

In order to compare the results of the present spatial BiGlobal analysis, as employed to an isolated Batchelor vortex, with those obtained by Mayer & Powell

[40] using local instability analysis, a vortex radius $a = (a_y^2 + a_z^2)^{1/2}$ was defined using the polar moments

$$a_y = \left[\left(\int \int \zeta (y - y_c)^2 dy dz \right) / \Gamma \right]^{\frac{1}{2}}, \quad a_z = \left[\left(\int \int \zeta (z - z_c)^2 dy dz \right) / \Gamma \right]^{\frac{1}{2}}, \tag{3}$$

with (y_c, z_c) denoting the position of the vortex centroids [20],

$$y_c = \frac{1}{\Gamma} \int \int y \zeta dy dz, \quad z_c = \frac{1}{\Gamma} \int \int z \zeta dy dz. \tag{4}$$

2.2.2 Inviscid point vortex methods

The equations that govern motion of free point vortices can be found in classical fluid mechanics texts [2]. The ordinary differential equations describing evolution of the vortex coordinates without considering axial velocity and after imposing symmetry along the Oxy plane are [32]

$$\left[\frac{\mathrm{d}y_i}{\mathrm{d}t}, \frac{\mathrm{d}z_i}{\mathrm{d}t} \right] = \frac{1}{2\pi} \sum_{j=1, i \neq j}^{N} \Gamma_j \frac{[z_j - z_i, y_i - y_j]}{(y_i - y_j)^2 + (z_i - z_j)^2} - \frac{1}{2\pi} \sum_{j=1}^{N} \Gamma_j \frac{[-z_j - z_i, y_i - y_j]}{(y_i - y_j)^2 + (z_i + z_j)^2} \tag{5}$$

The initial vortex locations are extracted from the three-dimensional steady base flow computed in the DNS on a plane of constant axial coordinate x and a standard 4^{th} order Runge-Kutta method is employed to advance (5) along t which, in the context of this simplified inviscid method, can be identified with the axial spatial coordinate, x, by assuming a constant unit axial free-stream velocity.

Circulation Γ_i is attached to the $i-$th point vortex, such that the initial circulation for N vortices can be computed as $\Gamma = \sum_{i=1}^{N} \Gamma_i$. The coordinates of the centroids y_c, z_c are then computed as

$$y_c = \sum_{i=1}^{N} \frac{\Gamma_i y_i}{\Gamma} \quad \text{and} \quad z_c = \sum_{i=1}^{N} \frac{\Gamma_i z_i}{\Gamma}, \tag{6}$$

which permits calculation of the vortex radius, $a = (a_y^2 + a_z^2)^{1/2}$ again from the polar moments, now defined as

$$a_y = \left[\sum_{i=1}^{N} \Gamma_i (y_i - y_c)^2 / \Gamma \right]^{\frac{1}{2}}, \quad \text{and} \quad a_z = \left[\sum_{i=1}^{N} \Gamma_i (z_i - z_c)^2 / \Gamma \right]^{\frac{1}{2}}. \tag{7}$$

2.3 Local linear stability theory

Local linear stability theory (LST), based on variants of the Navier-Stokes equations linearized around one-dimensional planar or axisymmetric profiles has been employed to identify instabilities at appropriately chosen locations in the wake. The Ansatz for the local linear perturbations, $\tilde{\mathbf{q}}_0$, is

$$\tilde{\mathbf{q}}_0(x_1, x_2, x_3, t) = \hat{\mathbf{q}}_0(x_2) \exp[\mathrm{i}(\alpha x_1 + \beta x_3 - \omega t)] + \text{c.c.}, \tag{8}$$

with $\hat{\mathbf{q}}_0 = (\hat{u}_0, \hat{v}_0, \hat{w}_0, \hat{p}_0)^T$ representing the vector of one-dimensional complex amplitude functions and *c.c.* denoting complex conjugation, such that the left-hand-side of equation (8) be real. In the present spatial framework employed, ω is taken to be a real angular frequency parameter, two-dimensional perturbations ($\beta = 0$) are assumed and the complex eigenvalue, α, and the associated eigenvectors, $\hat{\mathbf{q}}_0$, are sought. The real part of the eigenvalue, α_r, is related with the wavenumber of the eigenmode along the streamwise direction, while its imaginary part, α_i, is the growth/damping rate of the perturbation.

In a Cartesian coordinate system the coordinates (x_1, x_2, x_3) are respectively identified as the axial, normal and lateral spatial directions, (x, y, z), while in cylindrical coordinates they represent the axial, radial and azimuthal directions, (x, r, θ). Substituting (8) into the Navier-Stokes equations and linearizing leads to the Orr-Sommerfeld equation and to the system solved by Mayer and Powell [40], in Cartesian and axisymmetric coordinates, respectively. The spatial Orr-Sommerfeld equation has been solved at the plane of symmetry at several axial locations, while the linearized equations of motion in cylindrical coordinates have also been solved as a spatial eigenvalue problem in the vicinity of the vortex core, at the same axial locations as the Orr-Sommerfeld equation. The respective local linear perturbations, $\tilde{\mathbf{q}}_0$, have been compared with the functions extracted from the corresponding portions of the the two-dimensional global perturbations, $\tilde{\mathbf{q}}_1$, defined in the next section, in order to draw conclusions on the capability of the local analysis to describe instability in the problem at hand.

2.4 Spatial BiGlobal analysis

Spatial BiGlobal analysis is the analog of classic local spatial LST in which two inhomogeneous spatial directions, y and z, are resolved simultaneously while the axial direction, x, is considered locally homogeneous. The perturbation vector is assumed to be of the form

$$\tilde{\mathbf{q}}_1(x, y, z, t) = \hat{\mathbf{q}}_1(y, z) \exp[\mathrm{i}(\alpha x - \omega t)] + \text{c.c.}, \tag{9}$$

with $\hat{\mathbf{q}}_1 = (\hat{u}_1, \hat{v}_1, \hat{w}_1, \hat{p}_1)^T$ representing the vector of two-dimensional complex amplitude functions and *c.c.* denoting complex conjugation, such that the left-hand-side of equation (9) be real. A spatial framework has also been used in a global context: ω is taken to be a real angular frequency parameter, while the complex eigenvalue α, and the associated eigenvectors $\hat{\mathbf{q}}_1$ are sought. In a manner analogous with local theory, the real part of the eigenvalue α_r of the global mode is related with its wavenumber along the axial direction x, $\alpha_r = 2\pi/L_x$, while its imaginary part is the growth/damping rate. A negative value of α_i indicates exponential growth of $\tilde{\mathbf{q}}_1$ in space, while $\alpha_i > 0$ denotes decay of $\tilde{\mathbf{q}}_1$ in space.

By substitution of the decomposition of flow variables along with definition (9) into the LNSE equations, the two-dimensional partial-differential equation based eigenvalue problem (EVP) is obtained. The EVP is quadratic in the eigenvalue α, and is converted into a linear eigenvalue problem, which is larger in size by a factor equal to the degree of non-linearity (see [51]), using the companion matrix method [5], in which an auxiliary vector is defined, $\hat{\mathbf{q}}_1 = [\hat{u}_1, \hat{v}_1, \hat{w}_1, \hat{p}_1, \alpha\hat{u}_1, \alpha\hat{v}_1, \alpha\hat{w}_1]^T$.

The resulting EVP is

$$\mathbf{A}\hat{\mathbf{q}}_1 = \alpha \mathbf{B}\hat{\mathbf{q}}_1, \tag{10}$$

where the entries of matrices $\mathbf{A}$ and $\mathbf{B}$ are defined as

$$\mathbf{A} = \begin{pmatrix} \mathcal{L} & \bar{u}_y & \bar{u}_z & 0 & 0 & 0 & 0 \\ 0 & \mathcal{L}+\bar{v}_y & \bar{v}_z & \mathcal{D}_y & 0 & 0 & 0 \\ 0 & \bar{w}_y & \mathcal{L}+\bar{w}_z & \mathcal{D}_z & 0 & 0 & 0 \\ 0 & \mathcal{D}_y & \mathcal{D}_z & 0 & 0 & 0 & 0 \\ 0 & 0 & 0 & 0 & \mathcal{I} & 0 & 0 \\ 0 & 0 & 0 & 0 & 0 & \mathcal{I} & 0 \\ 0 & 0 & 0 & 0 & 0 & 0 & \mathcal{I} \end{pmatrix}, \quad \mathbf{B} = \begin{pmatrix} -\mathrm{i}\bar{u} & 0 & 0 & -\mathrm{i} & -\frac{1}{Re} & 0 & 0 \\ 0 & -\mathrm{i}\bar{u} & 0 & 0 & 0 & -\frac{1}{Re} & 0 \\ 0 & 0 & -\mathrm{i}\bar{u} & 0 & 0 & 0 & -\frac{1}{Re} \\ -\mathrm{i} & 0 & 0 & 0 & 0 & 0 & 0 \\ \mathcal{I} & 0 & 0 & 0 & 0 & 0 & 0 \\ 0 & \mathcal{I} & 0 & 0 & 0 & 0 & 0 \\ 0 & 0 & \mathcal{I} & 0 & 0 & 0 & 0 \end{pmatrix} \tag{11}$$

where $\mathcal{L} = -\mathrm{i}\omega + \bar{v}\mathcal{D}_y + \bar{w}\mathcal{D}_z - \frac{1}{Re}(\mathcal{D}^2_{yy} + \mathcal{D}^2_{zz})$, $\mathcal{D}_y = \partial/\partial y, \mathcal{D}^2_{yy} = \partial^2/\partial y^2, \mathcal{D}_z = \partial/\partial z$ and $\mathcal{D}^2_{zz} = \partial^2/\partial z^2$.

The results of spatial BiGlobal analysis are interesting in their own right, and are also used to obtain the shape function, wavenumber, and damping/growth-rate, required as initial conditions of the PSE-3D marching integration.

2.5 Linear PSE-3D

The PSE-3D instability analysis methodology is gaining acceptance as an tool for the prediction of linear and nonlinear instability of basic states with a mild variation in the streamwise coordinate and strong base flow gradients on the plane normal to the streamwise direction. Examples of successful application include vortical flows [9,10,47], the wake of an isolated roughness element in supersonic flow [13], streaks in a boundary layer [39], corner flows [17] and models of duct intakes [18]. The near and mid-field wake of the wing, where strong lateral flow gradients, in addition to a relatively milder flow dependence along the axial direction, make PSE-3D the method of choice for the instability analysis of this inhomogeneous flow field.

The Ansatz utilized to decompose the flow perturbations is based on the assumption that $\partial/\partial x \ll \partial/\partial y, \partial/\partial z$ and replaces (9) by

$$\tilde{\mathbf{q}}_2(x,y,z,t) = \hat{\mathbf{q}}_2(x,y,z) \exp\left[\mathrm{i}\int_x \alpha(x')dx' - \omega t\right] + \text{c.c.}. \tag{12}$$

Here $\hat{\mathbf{q}}_2$ is the amplitude function and α is the corresponding wavenumber, both varying slowly along the axial spatial direction. The real parameter ω denotes the frequency of the perturbations.

By substitution of the decomposition (12) into the LNSE equations, neglecting viscous terms with streamwise derivatives of $\mathcal{O}(Re^{-2})$ and higher, the linear PSE-3D equations can be obtained, written in a compact form as

$$\left(\mathbf{M} + \mathbf{N}\frac{\partial}{\partial x}\right)\hat{\mathbf{q}}_2(x,y,z) = 0. \tag{13}$$

The entries of the matrices $\mathbf{M}$ and $\mathbf{N}$ are

$$\mathbf{M} = \begin{pmatrix} \mathcal{M} + \bar{u}_x & \bar{u}_y & \bar{u}_z & \mathrm{i}\alpha \\ \bar{v}_x & \mathcal{M} + \bar{v}_y & \bar{v}_z & \mathcal{D}_y \\ \bar{w}_x & \bar{w}_y & \mathcal{M} + \bar{w}_z & \mathcal{D}_z \\ \mathrm{i}\alpha & \mathcal{D}_y & \mathcal{D}_z & 0 \end{pmatrix}, \quad \mathbf{N} = \begin{pmatrix} \bar{u} & 0 & 0 & 1 \\ 0 & \bar{u} & 0 & 0 \\ 0 & 0 & \bar{u} & 0 \\ 1 & 0 & 0 & 0 \end{pmatrix} \tag{14}$$

where $\mathcal{M} = \bar{u}\mathrm{i}\alpha + \bar{v}\mathcal{D}_y + \bar{w}\mathcal{D}_z - \frac{1}{Re}(\mathcal{D}_{yy}^2 - \mathcal{D}_{zz}^2 - \alpha^2) - \mathrm{i}\omega$ and, as in spatial BiGlobal theory, $\omega \in \mathbb{R}$ is a real frequency parameter and $\alpha \in \mathbb{C}$.

An ambiguity arises regarding the normalization condition which needs to be imposed in order to ensure, firstly, that the variation of the shape function along the streamwise direction be small and, secondly, that all amplitude growth be captured by the phase function. This issue has been discussed and resolved by Herbert [24, 25] in the context of the classic parabolized stability equations. The same concept is extended to PSE-3D, where the normalization condition

$$\int_{\Omega} \hat{\mathbf{q}}_2^{\dagger} \frac{\partial \hat{\mathbf{q}}_2}{\partial x} \, d\Omega = 0 \tag{15}$$

is used, where Ω denotes the extent of the computational domain on the plane normal to the axial spatial direction and superscript † denotes complex conjugate. Much like in the classic PSE, upstream propagating disturbances which are inherent to the parabolized (but not strictly parabolic) nature of the disturbance equations, are also found to be present in PSE-3D [7]. Here the remedy proposed by Li and Malik [36–38] is used, namely streamwise spatial integration of (13) using a marching step $\Delta x > 1/|\alpha|$.

A spatial amplification rate, σ, may be defined in the PSE-3D analysis as

$$\sigma = -\alpha_i + \frac{1}{2}\frac{d}{dx}\log E(x). \tag{16}$$

Here $E = \int_{\Omega}(\hat{u}\hat{u}^{\dagger} + \hat{v}\hat{v}^{\dagger} + \hat{w}\hat{w}^{\dagger})d\Omega$ is the kinetic energy of the perturbations, the latter being three-dimensional functions of the spatial coordinates that vary slowly along the axial direction. In a manner analogous with the classic PSE, the amplification rate in (16) is composed of two contributions, the local $-\alpha_i$ obtained at convergence of solution of (13) at each $x-$location to which the term corresponding to the perturbation kinetic energy is added.

3 Results

3.1 Base flow

Table 1 presents results of the base flow around the wing, computed by direct numerical simulation using the nek5000 code at $Re_c = 1750, AoA = 0^{\circ}$ and $AoA = 5^{\circ}$. At these conditions, $\Gamma = 0.033$ and 0.12, respectively; at the angle of attack $AoA = 5^{\circ}$ analyzed below, this corresponds to $Re = 210$. Shown in the table is the vorticity at a randomly selected location close to the trailing vortex core, as obtained on two meshes, $M1$ extending to $z = 2.5$ in the spanwise direction and comprising 16120 elements, and $M2$, extending to $z = 5$ and comprising 25312 elements. Two computations are performed at each angle of attack,

respectively using polynomial orders of $p = 4$ vs. 5 and $p = 5$ vs. 7. It can be seen that the relative error is of $O(1\%)$ in any of the three vorticity components, indicating a reasonable convergence of the base flow first derivatives, as required in the subsequent stability analysis. The vorticity distribution immediately behind the wing in the $AoA = 5^\circ$ case was used to initialize point-vortex simulations of the wake evolution. Equation (5) was advanced for forty non-dimensional time-units, which corresponds to an axial location well beyond that used in the DNS. This permitted comparisons between viscous and inviscid flow development within the domain resolved by the DNS and also revealed the long-time evolution of the inviscid counterpart of the flowfield.

Figure 2 shows a perspective view of the base flow obtained in the DNS as well as the inviscid counterpart of this flow obtained by the point-vortex method. Four features are highlighted in the DNS result: First, the system of trailing vortices and the vortex parallel to the trailing edge are outlined by the position of the respective vortex cores. Second, a number of surface streamlines indicate the position of primary separation on the wing surface, while some of these streamlines are shown to continue in the wake. Third, five equally spaced isolines of the flow vorticity magnitude in the range $0 \leq ||\nabla \times \mathbf{u}|| \leq 1$ are plotted on four planes located at $x = 6, 8, 10$ and 12. The subsequent global instability analysis will be performed on the planes shown in this figure for reasons that are explained shortly in the results of Figure 3. Finally, the left insert figure shows that steady laminar separation occurs on the wing at this set of parameters.

The result of the inviscid point vortex method is also shown in the right part of Figure 2. The vortex core lines in this image are those obtained in the DNS to which the result obtained by time-advancing Equation (5) is added, using the constant free-stream velocity to convert the time- to axial coordinate. It can be seen that, while there certainly exists a qualitative correspondence between the viscous and inviscid results, quantitative differences are also to be observed, especially as regards the vortex core location and size. The long-time evolution of the inviscid flow, obtained by integrating equation (5), reveals the development of instabilities in the entire wake. The result at $t = 40$, which approximately corresponds to a distance twice the axial length of the DNS computational domain, can be seen in the right insert figure and shows the development of instability in the vortex sheet as it rolls up. The complete time-evolution of the inviscid flow can be seen as supplementary material of this work.

A more quantitative description of the viscous base flow and its differences from its inviscid counterpart can be found in Figures 3 and 4. In the first, the dependence of the vertical y_c and lateral z_c coordinate of the trailing vortex core on the streamwise coordinate x is shown, as computed from equation (4). It can be seen that in the range $6 \leq x \leq 14$ the function $y(x)$ is approximately linear, indicating a constant downwash velocity. The latter quantity can be computed from these results and can be compared with analytic isolated vortex models on which the simpler (local) instability analysis is based. The point-vortex theory is precisely such a widely-used simplified model, the results of which for the vortex centroids, computed using equation (6), are included in Figure 3. Despite the relatively low Reynolds number of the DNS, a rather good agreement between the two sets of results can be observed.

Figure 4 shows results of application of equation (3) to compute the polar moments a_y and a_z using results of direct numerical simulation, as well as results

obtained from application of equation (7) to compute the polar moments in an inviscid framework. In both cases only the axial vorticity component has been used in the vicinity of the vortex. The agreement between viscous and inviscid polar moments is less favorable than that seen in the respective vortex centroid results of Figure 3. The values of the viscous polar moments can be seen to always exceed those of the respective inviscid quantities at all axial locations. As a consequence, at a given position x, the direct numerical simulation predicts a wider vortex than the one yielded by the inviscid analysis, differences increasing with increasing axial position. This result is not surprising, given the rather low Reynolds number value at which the DNS is performed.

3.2 Global modal analysis

3.2.1 Spatial BiGlobal instability analysis validation on the q−vortex

Validations of the global instability analysis algorithms utilized have been presented in the incompressible [46] and the compressible [13] flow regime. Here the performance of the code employed for the solution of the spatial BiGlobal eigenvalue problem is assessed by comparing results obtained on an isolated $q-$vortex model against the classic work of Mayer & Powell [40]; the main results are summarized below.

The $q-$vortex flow proposed by Lessen *et al.* [34,33] is a limit case of the Batchelor [3] vortex, when the dependence of the flowfield on the axial direction is neglected. In this case, the swirl parameter q, which is spatially-varying in the Batchelor vortex, is taken to be constant, $q = \Gamma/(2\pi U_c \delta)$, U_c being the core vortex velocity, U_0 the free-stream velocity and δ the core radius. The parallel-flow version of Batchelor vortex becomes

$$U_x = \frac{U_0}{U_c} + exp(-r^2), \quad U_r = 0, \quad U_\theta = \frac{q}{r}\{1 - exp(-r^2)\}, \tag{17}$$

where r is the radial distance from the vortex center. The Reynolds number in this case is defined as

$$Re = \frac{U_c \delta}{\nu} \tag{18}$$

The temporal stability problem pertinent to the base flow (17) was solved for the parameters addressed by Mayer and Powell [40], $q = 0.475$, $Re = 100$, $\frac{U_0}{U_c} = 0$ and axial wavenumber 0.418. The domain was truncated at $y_\infty = z_\infty = 40$ and the FD-q10 [2] spatial discretization method was used, alongside the classic spectral collocation based on the Chebyshev Gauss-Lobatto (CGL) nodes. Table 2 presents the convergence of the leading eigenvalue with increasing resolution and compares with the result of reference [40]. The eigenvalues converge to a value with absolute difference lower than 10^{-9} between the results of FD-q10 and CGL. Note that serial computation of the numerical solution of the temporal BiGlobal EVP using the highest resolution ($N = 71^2$) for CGL required 4935 Mbytes of memory, while in the case of FD-q10 ($N = 101^2$) the memory used was 1496 Mbytes, illustrating

[2] defined by Paredes *et al.*[44]

the performance improvement of the combination of high-order finite-difference schemes in conjunction with sparse storage and algebra [44].

These numerical efficiency improvements were crucial for the success of spatial BiGlobal EVP solutions, also performed for the $q-$vortex at $Re = 1200$ and $q = 0.8$. Temporal stability results for the same case were presented by González *et al.* [21]. Here, the spatial eigenvalue problem (10) was solved, employing FD-q10 spatial discretization method, alongside $N = 101^2$ collocation points along each of the simultaneously discretized spatial directions, y and z. Figure (5, left) shows the eigenspectrum at $\omega = -2$. A branch of eigenvalues appear for $\alpha_r = 0$ and $\alpha_i < 0$, which corresponds to a discretized spectrum of upstream moving pressure waves. This branch will be suppressed in the subsequent PSE-3D analysis in order to permit a stable numerical integration along the axial direction, as discussed by Li and Malik [37].

In addition, different branches of discrete eigenvalues are found, describing near-vertical lines. The discrete modes present a periodic structure in the azimuthal direction, with all the modes inside each branch having the same wavenumber m. Note that when local stability analysis based on the Orr-Sommerfeld equation in cylindrical coordinates is used, the wavenumber m is a parameter of the problem. The BiGlobal analysis recovers the results of several local analysis at the same time. The most unstable mode, which is found to be in good agreement with the result presented in [21], is noted by full symbol in the spectrum shown in Figure (5, left), while the spatial structure of its streamwise velocity component, $\hat{u}(y, z)$, is shown in Figure (5, right).

3.2.2 Spatial BiGlobal analysis in the wake of a three-dimensional wing

Having validated the algorithms on a relevant problem, attention is turned next to the main topic of the present article, namely instability analysis in the wake of a short aspect-ratio three-dimensional wing using global linear analysis methods. Planes of data at constant $x = 6, 8, 10$ and 12 in the region of constant downwash were extracted from the three-dimensional base flow fields computed by DNS in Section 3.1 and the spatial global EVP (10) was solved at non-dimensional frequencies in the band $\omega \in [0, 12]$. Half of the computational domain was resolved using FD-q6 spatial discretization, on rectangular domains discretized by $(Ny = 101) \times (Nz = 161)$ and $(Ny = 161) \times (Nz = 201)$ collocation points. All subsequent results were obtained using the lower resolution, which was found to be sufficient for convergence. Two classes of boundary conditions, symmetric and antisymmetric, were imposed at the symmetry boundary on all perturbation components, alongside homogeneous Dirichlet conditions on all other domain boundaries.

Figure 6 presents the dependence of the spatial amplification rate, $-\alpha_i$, on the wavenumber α_r at the conditions examined. Both symmetric and antisymmetric disturbances are found to be linearly unstable over a wide range of wavenumbers. In both classes of disturbances the entire amplified branch is damped as the downstream distance from the wing decreases. It can also be clearly seen that the symmetric perturbations are substantially more amplified than their antisymmetric counterparts. Results of the spatial Orr-Sommerfeld equation added to this figure will be discussed in detail in Section 3.4.1.

Figure 7 compares the amplitude functions of the linear symmetric and antisymmetric perturbations at a single downstream location, $x = 10$ and frequencies near the respective maximally amplified, $\omega = 5.5$ and $\omega = 5$. Shown are the real and imaginary parts of the amplitude functions of the perturbation velocity vector. In all plots the amplitude functions are normalized with respect to their maxima and are shown as greyscale isosurfaces superposed upon the respective underlying base flow. The latter is made visible through four isolines of the streamwise velocity component between the values $0.8 \leq \bar{u}(x_0; y, z) \leq 0.95$. It can be seen that both of the more feeble antisymmetric perturbations and the stronger amplified symmetric perturbations mainly affect the vortex sheet connecting the two trailing vortices.

3.3 Linear PSE-3D analysis

3.3.1 PSE-3D analysis validation on the Batchelor vortex

PSE-3D analysis permits considering a basic state which depends mildly on one and strongly on the other two spatial directions. An isolated non-parallel Batchelor vortex has been computed using the Parabolized Navier Stokes (PNS) formulation in cylindrical coordinates discussed by Paredes *et al.* [45]. The selected initial conditions are swirl strength parameters $\kappa_0 = 0.8$ and axial velocity defect $\gamma_0 = 0.8$. The Reynolds number based on the initial vortex radius and free-stream velocity is set to $Re = 3000$, and the disturbance frequency is $\omega = 4.6$; additional details provided in [45,43].

Figure 8 shows the evolution of the spatial growth rate, $-\alpha_i$, along the axial direction computed using PSE-3D and conventional PSE with cylindrical coordinates [45]. Excellent agreement exists between the results delivered by both methodologies. Shown also in this figure are results of the classic local stability analysis, which are seen to strongly deviate from those of both PSE methodologies. For example at $x = 10$, a discrepancy in amplification rate larger than 50 % is observed. However, it is interesting to note that, although large discrepancies exist between the two sets of results, both curves cross the neutral stability threshold, $\alpha_i = 0$, at same axial position $x \approx 25.4$.

3.3.2 PSE-3D analysis in the wake of a three-dimensional wing

In the problem at hand, the PSE-3D marching procedure is initialized using results of the respective spatial eigenvalue problem at $x = 6$ for either symmetric or antisymmetric modes. The spatial integration is advanced until $x = 14$ for a frequency range of $\omega \in [3, 8]$ in steps of $\Delta\omega = 0.5$, which encompasses the maximally amplified modes predicted by the spatial BiGlobal analysis, previously shown in Figure 6. Figure 9 presents the streamwise evolution of the kinetic energy of symmetric and antisymmetric perturbations, respectively denoted by full and open symbols, normalized using the perturbation energy at $x = 6$. The respective frequencies of the maximally amplified perturbations can be seen in this figure. Results of Figure 9 show that linear PSE-3D analysis also predicts that symmetric disturbances are more strongly amplified than their antisymmetric counterparts. N-factors, not shown here for brevity, have been computed on the basis of these results and can

be used to make predictions as regards linear breakdown and transition of the computed perturbations. An 8-fold increase in magnitude of the symmetric perturbation initial energy requires an axial distance $x = O(100)$ downstream of the wing.

The distribution of the spatial amplification rate, σ, is compared with the imaginary part of the eigenvalue, $-\alpha_i$, obtained in the spatial BiGlobal analysis in Figure 10, in which the (identical with the spatial eigenvalue problem solution) initialization data for the PSE-3D at $x = 6$ is not included. Two noteworthy observations are made. First, the most amplified frequency range delivered by the linear PSE-3D analysis is slightly lower than that predicted by the spatial BiGlobal eigenvalue problem solution. Second, the difference in the predictions of the two methodologies diminishes as x increases. As discussed in sections 2.4 and 2.5, the global eigenvalue problem assumes independence of the base flow of the axial spatial direction, while PSE-3D assumes a weak viscous spreading. If the wake width, $\delta \propto \sqrt{x}$, is taken as a measure of viscous spreading [48], then $d\delta(x)/dx \propto x^{-\frac{1}{2}}$. The latter quantity diminishes as x increases, which is consistent with the diminishing of the differences in the predictions of the spatial BiGlobal eigenvalue problem and the linear PSE-3D marching procedure.

Figure 11 compares the evolution of the magnitude of the symmetric and antisymmetric streamwise perturbation velocity obtained by linear PSE-3D analysis at the maximally amplified frequencies, $\omega = 6.0$ and $\omega = 5.0$, respectively. Consistently with the previous results the respective eigenfunctions peak at the vortex sheet between the two vortices over the entire range of axial locations examined.

3.4 Comparisons with local linear theory

3.4.1 Wake profiles at the plane of symmetry

Results of both of the spatial BiGlobal and the linearized PSE-3D analyses show that, at the conditions examined, a symmetric instability which peaks at the plane of symmetry is the leading linear perturbation of the steady laminar flow in the wake of the wing. It thus becomes interesting to examine whether application of classic linear local instability analysis to the streamwise velocity profile at the plane of symmetry can deliver reliable predictions of the physics of linear instability. This question has been answered by extracting streamwise velocity profiles $\bar{u}(y)$ from the steady laminar base flow computed by DNS. Profiles were extracted at the plane of symmetry $z = 0$ and the same streamwise locations $x = 6, 8, 10$ and 12 at which spatial BiGlobal analyses have also been performed. At those locations the spatial Orr-Sommerfeld equation has been solved to determine the most unstable local linear instabilities. The results have been shown as solid lines in Figure 6, where the solution of the spatial BiGlobal eigenvalue problem (10) at the same locations is also shown as symbols. Comparisons of the two sets of results at all axial positions leads to a two-fold conclusion.

Qualitatively, the spatial Orr-Sommerfeld equation is capable of predicting the characteristics of the (convective) instability at this part of the domain. The range of amplified linear perturbation frequencies as well as the frequency of the most amplified modal perturbation are reasonably well captured by the simple (and

substantially less expensive) local analysis method. However, if quantitative predictions are sought for the amplification rates, the $O(30\%)$ differences between the results of the local and global analyses suggests that the usefulness of the Orr-Sommerfeld equation may be limited in this respect. This may be attributed to the closeness of the vortex pair to the midplane of symmetry, which invalidates the assumption of spanwise base flow homogeneity, as employed in the Orr-Sommerfeld equation. Interestingly, the modulus of the amplitude function of the leading eigenmode delivered by local theory, $\hat{u}_0(y)$, and that of a cut through the two-dimensional streamwise component of the eigenvector delivered by the global analysis, $\hat{u}_1(x = 10, y, z = 0)$ are seen in Figure 12 to be in rather close agreement. Figure 12 also presents isosurfaces of the composite flow field at the symmetry plane, reconstructed according to the local linear theory Ansatz. To this end, the leading eigenmode of the Orr-Sommerfeld equation has been superposed to the underlying streamwise velocity component at a linearly small amplitude. The resulting flow shows the typical cats-eyes pattern of wake instability which, in the context of local theory, is periodic by construction along the axial direction. However, the rather large difference between the predictions on amplification delivered by spatial BiGlobal and linear PSE-3D analysis suggests that neither the local theory nor the spatial BiGlobal analysis should be employed to analyze instability in the near-mid-field of low-aspect ratio wings at low Reynolds numbers. Instead, the linear PSE-3D methodology, which incorporates all relevant features of the underlying base flow should be employed if quantitative predictions are sought.

A final interesting observation can be made by comparing results presented in Figures 6 and 10, namely the approximate, but not exact as in temporal theory, proportionality of the frequency, ω, and α_r in spatial BiGlobal analysis, or σ in the linear PSE-3D. Much like the spatial local theory prediction of Michalke [42] in his classic work on the hyperbolic tangent profile, and unlike the corresponding temporal theories, in the wake configuration behind the wing too, both spatial BiGlobal and linear PSE-3D analyses deliver approximately, but not exactly constant phase velocities, ω/α_r.

3.4.2 Local analysis near the vortex core

Linear local instability of the vortex at the axial location $x = 10$ has been performed by solving the axisymmetric counterpart of the spatial Orr-Sommerfeld equation [40] for a base velocity profile centered at the vortex centroid and extending radially outward. A number of eigenmodes were identified in the frequency range $\omega \in [0, 8]$ and azimuthal wavenumbers $m \in [0, 10]$. The mode $m = 2$ is maximally amplified at a frequency $\omega \approx 6$, having a spatial amplification of $-\alpha_i \approx 3.2 \times 10^{-2}$, as can be seen in Figure 13. The amplitude functions also shown in this figure correspond by construction[3] to a purely axisymmetric eigenfunction with two positive and two negative peaks, as implied by the azimuthal wavenumber parameter.

Perhaps the most interesting aspect of these results is that the local analysis in the vicinity of the vortex core also predicts a maximally amplified frequency which peaks around $\omega = 6$, consistently with what has been found by the spatial

[3] c.f. Equation (8)

Orr-Sommerfeld equation at the plane of symmetry and by both global approaches on the entire domain. However, unlike the result of the local analysis in the wake, an axisymmetric eigenmode structure near the vortex core is not to be seen in the amplitude functions of the global analyses shown in Figures 7 and 11. This may be attributed to the fact that instability in the vortex sheet is inviscid in nature and is expected to be the defining characteristic of the leading linear perturbation of the present base flow, independently of the analysis approach used. By contrast, the viscous instability in the vortex core has orders-of-magnitude lower amplification rates than the instability peaking at the symmetry plane and, as such, the global eigenvalue spectrum is dominated by instability in the wake.

Finally, it should be mentioned that the wake will not only develop inviscid instabilities in the Oxy plane due to the inflectional velocity profile in the x direction. This type of instabilities will also appear on Oyz planes too, as an inflectional velocity profile is also to be found along the z direction at some point between the axis of symmetry and the vortex core. This feature is captured by the point-vortex simulations as has already been seen in the insert Figure 2. However, complete description of all linear instability mechanisms beyond the leading perturbations identified by global methods is beyond the scope of the present work.

4 Discussion

The present work addresses questions that were opened at the turn of the century, during the large-scale pan-European R& D efforts surrounding the introduction of the A380. At that time analysis approaches ranging from point vortices to direct numerical simulation were employed to understand the so-called 'near-midfield' behind wings of various shapes. The then nascent global instability had been demonstrated for vortical flows but, at that time, had not reached the level of maturity in order to become an alternative to the established inviscid (and viscous) point-vortex methods and local linear instability analyses. The present work intends to revive some of these questions and demonstrate that global analysis is not only feasible for full wing configurations, but also delivers results that are qualitatively close but quantitatively different from those of the simplified approaches.

Here, linear global instability analysis of the trailing vortex system behind a low aspect ratio three-dimensional wing has been performed by solving the spatial BiGlobal eigenvalue problem, as well as by employing the linear PSE-3D disturbance equations. To the authors' knowledge both approaches are used for the first time to analyze a flow of this class. At the low Reynolds number examined, two classes of disturbances have been discovered, symmetric perturbations corresponding to instability of the vortex sheet connecting the system of trailing vortices and antisymmetric perturbations peaking at the vortex sheet and also in the neighborhood of the vortex cores. The global modes discovered are shown in Figure 14 in a perspective view showing isosurfaces of the streamwise perturbation velocity, alongside the base flow vortex core positions.

The global analysis results obtained are consistent with the physical understanding of instability in the wake of a short aspect ratio wing. A larger growth of linear instabilities at the plane of symmetry leads to earlier destruction of the coherence of the vortex sheet, while lower levels of the (two-dimensional) amplitude functions in the vicinity of the vortex suggest that the trailing-vortex system per-

sists for axial distances longer than the $20b$ presently examined. In other words, the wake (shear) destruction, does not imply destruction of the trailing-vortex system, such that the vortex wake hazard persists after destruction of the vortex sheet by linear instability mechanisms. From a physical point of view the earlier destruction of the vortex sheet can be attributed to the inflectional nature of the profiles at the wake portion near the symmetry plane, while the persistence of the trailing vortex system is due to the viscous nature of vortex instabilities. The early destruction of the vortex sheet is corroborated in the inviscid limit by the point-vortex method employed, results of which show that the trailing vortex system persists for substantially longer axial distances beyond that at which linear instability of the wake develops.

Qualitative agreement has been obtained between results delivered by global and local linear instability analyses regarding the dominant linear mechanism in the wake. However, the spatial Orr-Sommerfeld equation applied to wake velocity profiles at the plane of symmetry largely overpredicts the amplification rates delivered by the spatial BiGlobal eigenvalue problem or the linear PSE-3D marching approach. On the other hand, more work will be necessary in order to identify instability in the vortex core which, owing to its viscous nature, will be less significant from a linear analysis perspective compared to the wake mode identified by solution of both the spatial BiGlobal eigenvalue problem and linear PSE-3D analysis.

Overall, the main contribution of the present work is the demonstration that application of inviscid point-vortex and viscous local, BiGlobal and linear PSE-3D analyses to analyze instability in the wake of a low aspect ratio wing at low Reynolds number are all capable of offering a qualitative consistent picture of the physics of active linear instability mechanisms, namely early destruction of the vortex sheet and persistence of the trailing vortex system. However, quantitatively different predictions of amplification rates of linear perturbations and their respective frequencies are obtained by each analysis methodology. Since only PSE-3D incorporates all necessary features of the underlying base flow field, namely viscosity, strong lateral velocity gradients and weak base flow development along the axial direction, while all other analysis methodologies (except DNS) need to make simplifying assumptions regarding the underlying base flow, it must be concluded that linear instability analyses in the problem at hand need to employ the PSE-3D methodology. The conclusions drawn are specific to the configuration chosen at the low Reynolds number addressed and should not be taken as a universal criterion for breakdown of the coherence of the wake behind the wing, but rather as a demonstration of the capability of the proposed analysis approach to deliver predictions without resorting to the simplifying assumptions on the form of the vortex system. Work in progress addresses larger aspect-ratio wings and a more relevant to flight higher Reynolds number, at which experiments are easier to perform; results will be reported in due course.

Acknowledgements The authors wish to thank Prof. Yuri Kachanov for introducing us to this problem and for sharing the short aspect ratio wing configuration and preliminary experimental results. Access to the Copper Cray XE6m (https://www.ors.hpc.mil) was made possible by project AFVAW10102F62, with Dr. Nicholas Bisek as Principal Investigator, and is gratefully acknowledged.

Table 1 Convergence study of vorticity components at the location $(x, y, z) = (12, 0, -0.85)$, close to the vortex core, at $Re_c = 1750$

AoA		ω_x	ω_y	ω_z	ω_x	ω_y	ω_z
			$p = 5$			$p = 7$	
$0°$	$M1$	0.0287	-0.1559	-0.0306	0.0286	-0.1557	-0.0307
	$M2$	0.0289	-0.1565	-0.0299	0.0289	-0.1563	-0.0299
			$p = 4$			$p = 5$	
$5°$	$M2$	0.1392	-0.3310	-0.0718	0.1385	-0.3407	-0.0708

Table 2 Temporal BiGlobal instability analysis of the $q-$vortex flow at $q = 0.475$, $Re = 100$ and $\beta = 0.418$. MP denotes the result of Mayer & Powell [40]

Discretization	N^2	$\omega_r \times 10^{-2}$	$\omega_i \times 10^{-3}$
CGL	20^2	2.833	9.64
	30^2	2.8352	9.617
	50^2	2.8351897	9.6169098
	70^2	2.835189660	9.616909850
FD10	40^2	2.8353	9.617
	60^2	2.8351899	9.61698
	80^2	2.8351895	9.616913
	100^2	2.83518965	9.61690986
MP			9.61

References

1. Ashworth, R., Mughal, S.: Modeling three dimensional effects on cross flow instability from leading edge dimples. Procedia IUTAM **14**, 201–210 (2015)
2. Batchelor, G.: An Introduction to Fluid Dynamics. Cambridge University Press (1967)
3. Batchelor, G.K.: Axial flow in trailing line vortices. J. Fluid Mech. **20**(4), 645–658 (1964)
4. Benton, S.I., Bons, J.P.: Three-dimensional instabilities in vortex/wall interactions: Linear stability and flow control. In: 52nd Aerospace Sciences Meeting. AIAA Paper 2014-1267, 13 - 16 January 2014, National Harbor, Maryland, USA (2014)
5. Bridges, T., Morris, P.: Differential eigenvalue problems in which the parameter appears nonlinearly. J. Comp. Phys. **55**, 437–460 (1984)
6. Brion, V., Sipp, D., Jacquin, L.: Optimal amplification of the crow instability. Phys. Fluids **19**, 111703 (2007)
7. Broadhurst, M., Sherwin, S.: The parabolised stability equations for 3d-flows: implementation and numerical stability. Applied Numerical Mathematics **58**(7), 1017–1029 (2008)
8. Broadhurst, M., Theofilis, V., Sherwin, S.J.: Spectral element stability analysis of vortical flows. In: R. Govindarajan (ed.) 6th IUTAM Symposium on Laminar-Turbulent Transition, pp. 153–158. Springer, 13-17 December 2004, Bangalore, India (2006)
9. Broadhurst, M., Theofilis, V., Sherwin, S.J.: Spectral element stability analysis of vortical flows. pp. 153–158. 6th IUTAM Laminar-Turbulent Transition Symposium, Bangalore, India, Dec. 2004 (2006)
10. Broadhurst, M.S., Sherwin, S.J.: The parabolised stability equations for 3D-flows: implementation and numerical stability. Appl. Num. Math. **58**, 1017–1029 (2008)
11. Crouch, J.D.: Instability and transient growth for two trailing-vortex pairs. J. Fluid Mech. **350**, 311–330 (1997)
12. Crow, S.C.: Stability theory for a pair of trailing vortices. AIAA J. **8**, 2172–2179 (1970)
13. De Tullio, N., Paredes, P., Sandham, N.D., Theofilis, V.: Laminar-turbulent transition induced by a discrete roughness element in a supersonic boundary layer. J. Fluid Mech. **735**, 613–646 (2013)
14. Duck, P.W.: On the downstream development and breakup of systems of trailing-line vortices. Theor. Comp. Fluid Dyn. **25**(1), 43–52 (2011)
15. Fabre, D., Jacquin, L.: Stability of a four-vortex aircraft wake model. Phys. Fluids **12**(10), 2438–2443 (2000)
16. Fischer, P.F., Lottes, J.W., Kerkemeier, S.G.: nek5000: http://nek5000.mcs.anl.gov (2008)
17. Galionis, I., Hall, P.: Spatial stability of the incompressible corner flow. Theor. Comp. Fluid Dyn. **19**, 77–113 (2005)
18. Galionis, I., Hall, P.: Stability of the flow in a slowly diverging rectangular duct. J. Fluid Mech. **555**, 43–58 (2006)
19. Gallaire, F., Chomaz, J.M.: Three-dimensional instability of isolated vortices. Phys. Fluids **15**(8), 2113 – 2126 (2003)
20. Gonzalez, L.M., Gomez-Blanco, R., Theofilis, V.: Eigenmodes of a counter-rotating vortex dipole. AIAA J. **46**(11), 2796–2805 (2008)
21. González, L.M., Theofilis, V., Meseguer, F.: Galerkin methods for biglobal linear instability analysis of vortical flows. In: Lecture Notes in Computational Science and Engineering. ICOSAHOM 09, 22-26 June, Trondheim, Norway. Springer (2009)
22. Heaton, C.J., Nichols, J.W., Schmid, P.J.: Global linear stability of the non-parallel batchelor vortex. J. Fluid Mech. **629**, 139–160 (2009)
23. Hein, S., Theofilis, V.: On instability characteristics of isolated vortices and models of trailing-vortex systems. Comp. & Fluids **33**(5-6), 741–753 (2004)
24. Herbert, T.: Parabolized stability equations. AGARD Report No. 793. Special Course on Progress in Transition Modelling pp. 4(1)–4(34) (1994)
25. Herbert, T.: Parabolized stability equations. Ann. Rev. Fluid Mech. **29**, 245–283 (1997)
26. Higuchi, H., Quadrelli, J.C., Farell, C.: Vortex roll-up from an elliptic wing at moderately low reynolds numbers. AIAA J. **25**(12), 1537–1542 (1987)
27. Jacquin, L., Fabre, D., Sipp, D., Theofilis, V., Vollmers, H.: Instability and unsteadiness of aircraft wake vortices. Aerosp. Sci. Technol. **7**(8), 577–593 (2003)
28. Jiménez, J.: Stability of a pair of co-rotating vortices. Phys. Fluids **18 (11)**, 1580–1581 (1970)
29. Kármán, T.V.: Über den Mechanismus des Widerstandes, den ein bewegter Körper in einer Flüssigkeit erfährt. Nachr. Ges. Wissenschaft. Göttingen pp. 509–517 (1911)

30. Kármán, T.V.: Über den Mechanismus des Widerstandes, den ein bewegter Körper in einer Flüssigkeit erfährt. Nachr. Ges. Wissenschaft. Göttingen pp. 547–556 (1912)
31. Lacaze, L., Ryan, K., Dizes, S.L.: Elliptic instability in a strained batchelor vortex. J. Fluid Mech. **577**, 341–361 (2007)
32. Leonard, A.: Vortex methods for flow simulation. J. Comp. Phys. **37**, 289–335 (1980)
33. Lessen, M., Paillet, F.: The stability of a trailing line vortex. part 2. viscous theory. J. Fluid Mech. **65**, 769–779 (1974)
34. Lessen, M., Singh, P.J., Paillet, F.: The stability of a trailing line vortex. part 1. inviscid theory. J. Fluid Mech. **63**, 753–763 (1974)
35. Leweke, T., Williamson, C.: Cooperative elliptic instability of a vortex pair. J. Fluid Mech. **360**, 85–119 (1998)
36. Li, F., Malik, M.: Mathematical nature of parabolized stability equations. R. Kobayashi (Ed.), Laminar-Turbulent Transition, Springer pp. 205–212 (1994)
37. Li, F., Malik, M.: On the nature of the pse approximation. Theoretical and Computational Fluid Dynamics **8**, 253–273 (1996)
38. Li, F., Malik, M.: Spectral analysis of parabolized stability equations. Compt. Fluids **26 (3)**, 279–297 (1997)
39. Martín, J., Paredes, P.: Three-dimensional instability analysis of boundary layers perturbed by streamwise vortices. Theor. Comp. Fluid Dyn. p. (in review) (2016)
40. Mayer, E.W., Powell, K.G.: Viscous and inviscid instabilities of a trailing vortex. J. Fluid Mech. **245**, 91–114 (1992)
41. Meunier, P., Leweke, T.: Elliptic instability of a co-rotating vortex pair. J. Fluid Mech. **533**, 125–159 (2005)
42. Michalke, A.: On spatially growing disturbances in an inviscid shear-layer. J. Fluid Mech. **23**(3), 521–544 (1965)
43. Paredes, P.: Advances in global instability computations: from incompressible to hypersonic flow. Phd thesis, Technical University of Madrid (2014)
44. Paredes, P., Hermanns, M., Le Clainche, S., Theofilis, V.: Order 10^4 speedup in global linear instability analysis using matrix formation. Comput. Meth. Appl. Mech. Eng. **253**, 287–304 (2013)
45. Paredes, P., Rodríguez, D., Theofilis, V.: Three-dimensional solutions of trailing-vortex flows using parabolized equations. AIAA J. **51**(12), 2763–2770 (2013)
46. Paredes, P., Theofilis, V., Rodríguez, D., Tendero, J.A.: The pse-3d instability analysis methodology for flows depending strongly on two and weakly on the third spatial dimension. In: 6th AIAA Theoretical Fluid Mechanics Conference. AIAA Paper 2011-3752, 27 - 30 June 2011, Honolulu, Hawaii, USA (2011)
47. Paredes, P., Theofilis, V., Rodríguez, D., Tendero, J.A.: The PSE-3D instability analysis methodology for flows depending strongly on two and weakly on the third spatial dimension. 6^{th} Theoretical Fluid Mechanics Conference, Honolulu, HI, June 27-30, 2011, AIAA Paper 2011-3752 (2011)
48. Schlichting, H.: Boundary Layer Theory. McGraw-Hill (1979)
49. Tendero, J.A., Paredes, P., Roura, M., Govindarajan, R., Theofilis, V.: BiGlobal and point vortex methods for the instability analysis of wakes. In: 31st AIAA Applied Aerodynamics Conference. AIAA Paper 2013-2820, June 24-27, 2013, San Diego, CA (2013)
50. Tendero, J.A., Theofilis, V., Roura, M., Govindarajan, R.: On vortex filament methods for linear instability analysis of aircraft wakes. Aerosp. Sci. Technol. **44**, 51–68 (2015)
51. Theofilis, V.: Spatial stability of incompressible attachment line flow. Theor. Comput. Fluid Dyn. **7**, 159–171 (1995)
52. Theofilis, V.: Global linear instability. Annu. Rev. Fluid Mech. **43**, 319–352 (2011)
53. Thomas, P.J., Auerbach, D.: The observation of the simultaneous development of a long- and a short-wave instability mode on a vortex pair. J. Fluid Mech. **265**, 289–302 (1994)
54. Xue, D., Pan, C., Wang, J., Borodulin, V.I., Kachanov, Y.S.: Determining time-scale of laminar wing-tip vortex instability by visualization. In: Proc. 13td Asian Symposium on Visualization, Khristianovich Institute of Theoretical and Applied Mechanics. Russian Academy of Sciences, Siberian Branch, Novosibirsk, Russia, June 22-26 (2015)

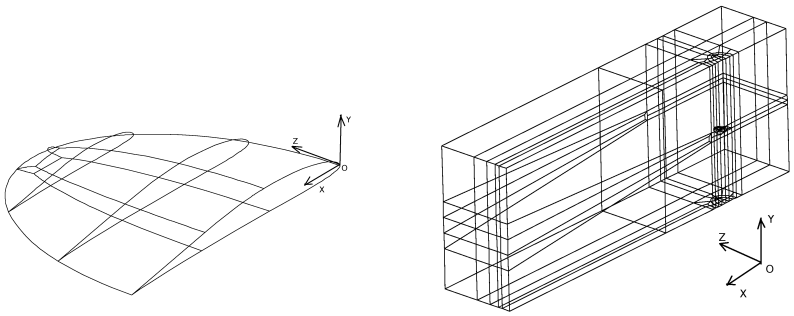

Fig. 1 *Left:* Perspective view of the E387 elliptic wing. *Right:* Full view of the computational domain, showing the macro-elements structure

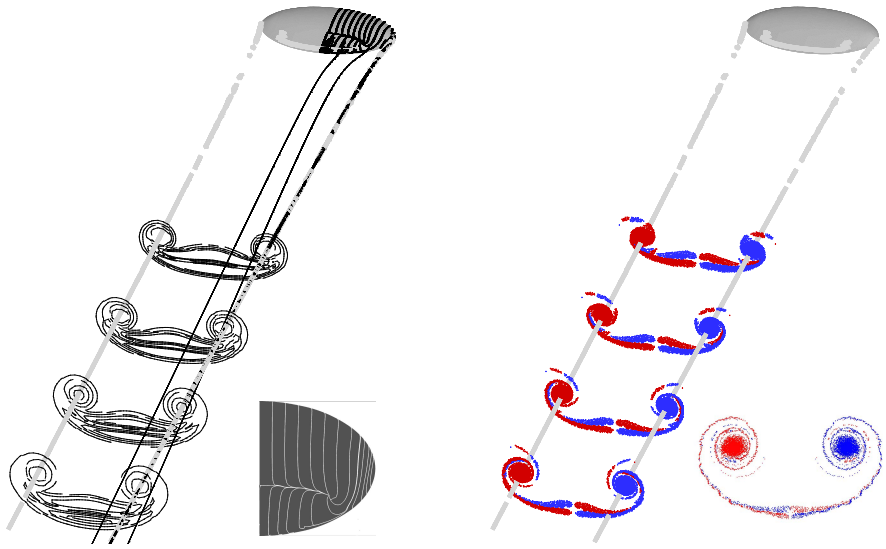

Fig. 2 *Left:* Three-dimensional perspective of the DNS-obtained steady laminar base flow over the wing at $Re_c = 1750$, $AoA = 5°$. *Right:* Same for the flow obtained by inviscid point-vortex methods, vortex core lines being those obtained in the DNS. Wall streamlines show laminar separation on the wing surface (*left insert*) and inviscid instability developing in the wake at $x = 40$ (*right insert*)

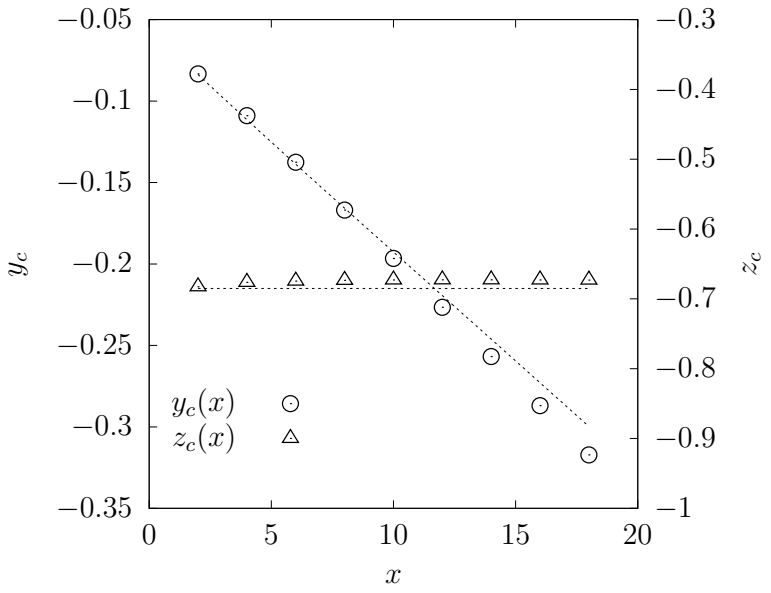

Fig. 3 Dependence of the normal, y_c, and lateral, z_c, spatial coordinates of the trailing vortex centroids on the streamwise coordinate, x. Symbols correspond to calculations using equation (4) applied to the DNS data and lines to calculations using equation (6) applied to data generated by the inviscid point-vortex method.

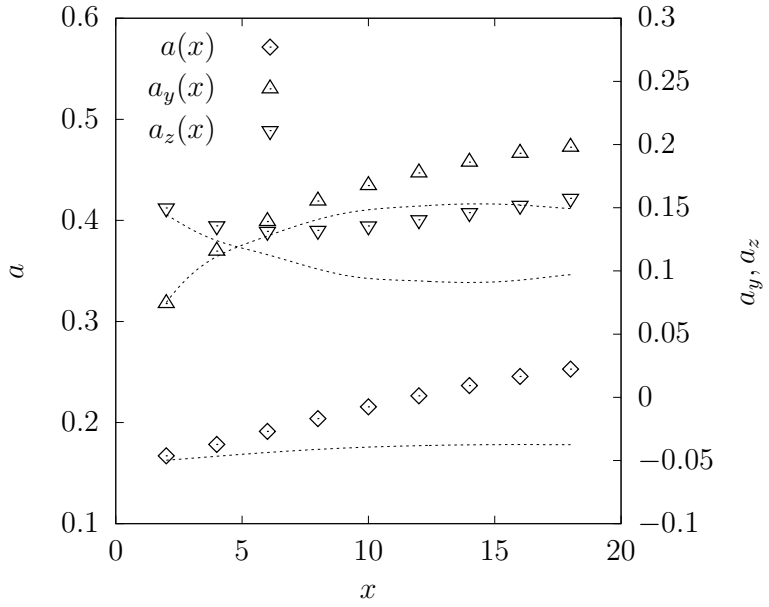

Fig. 4 Dependence of the polar moments, a_y, a_z, and vortex radius, a, on the streamwise coordinate, x. Symbols correspond to calculations using equation (3) applied to the DNS data and lines to calculations using equation (7) applied to data generated by the inviscid point-vortex method.

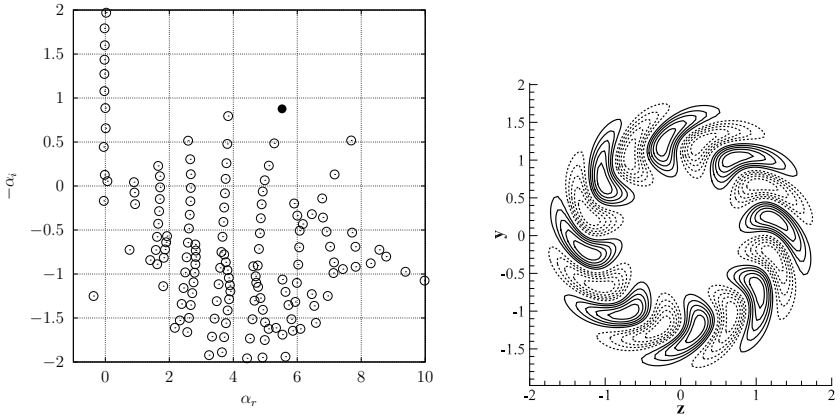

Fig. 5 *Left:* Eigenspectrum of the $q-$vortex at $Re = 1200$, $q = 0.8$ and $\omega = -2.0$. Full symbol denotes the most unstable mode of this family that corresponds to a eight lobes ($m = 8$) eigenmode. *Right:* The pertinent eigenfunction of this mode is plotted with contours (-0.9:0.1:0.9) of normalized real part of axial velocity amplitude function. Dashed lines correspond to negative values

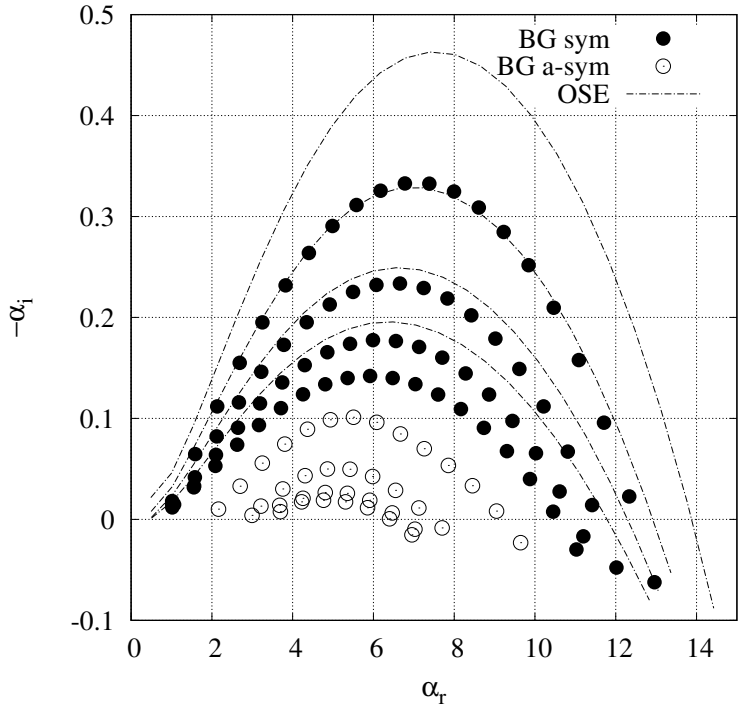

Fig. 6 Spatial amplification $-\alpha_i$ as a function of the wavenumber α_r for the two classes of boundary conditions, ●: symmetric; ○: anti-symmetric, obtained by solution of the spatial BiGlobal EVP (10). Results of the spatial Orr-Sommerfeld equation are also shown. In all three sets of results the axial range analyzed is $x \in [6, 12]$. The most-/least-amplified results correspond to $x = 6$ and $x = 12$, respectively

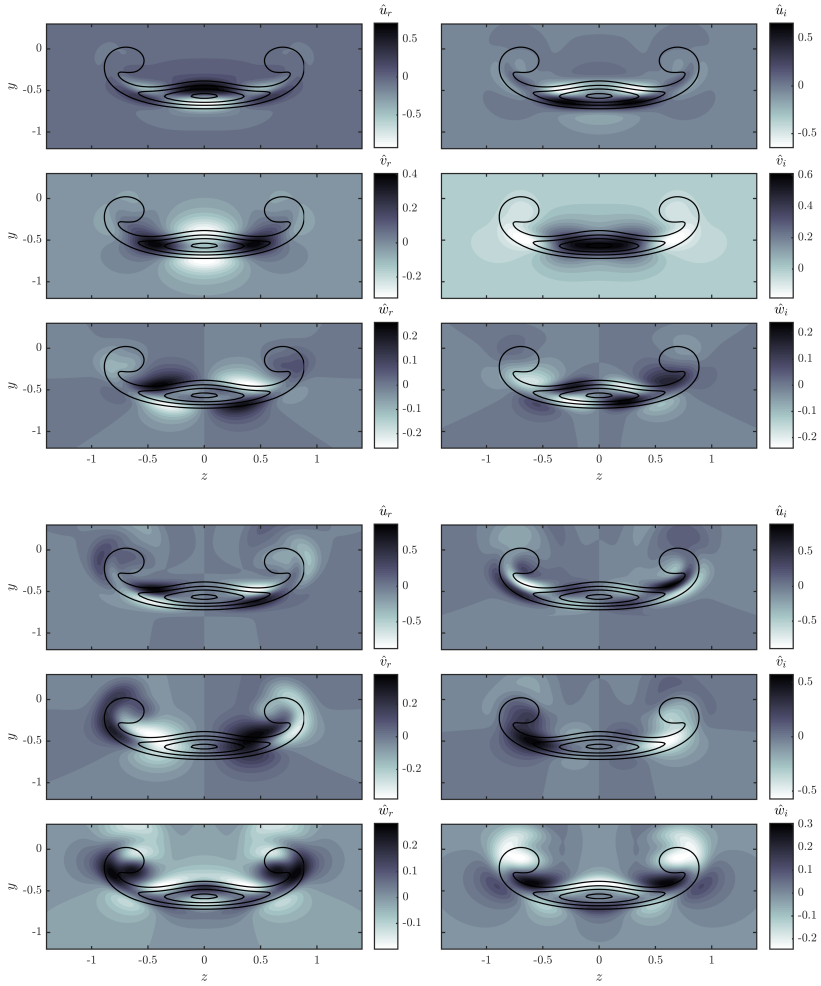

Fig. 7 Amplitude functions of the perturbation velocity components $\hat{\mathbf{q}}_1(y, z)$ resulting from solution of (10) at $x = 10$ and imposition of symmetric boundary conditions at $\omega = 5.5$ (upper) and the antisymmetric boundary conditions at $\omega = 5$ (lower). In the background isolines of the streamwise component of the base flow velocity are shown

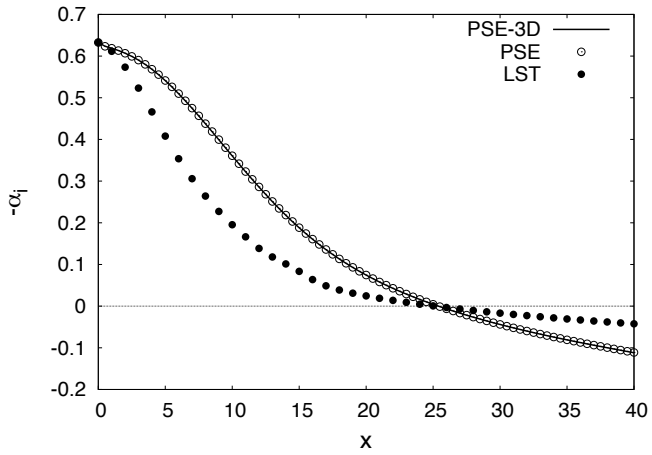

Fig. 8 Evolution of amplification rate for the non-parallel vortex flow ($\kappa_0 = 0.8$, $\gamma_0 = 0.8$) for the most unstable eigenmode at the selected parameters ($Re = 3000$, $\omega = 4.6$), comparing conventional PSE with cylindrical coordinates and PSE-3D results for a cross-validation test. Also, the leading eigenmode at each station is computed by local analysis (LST) [45]

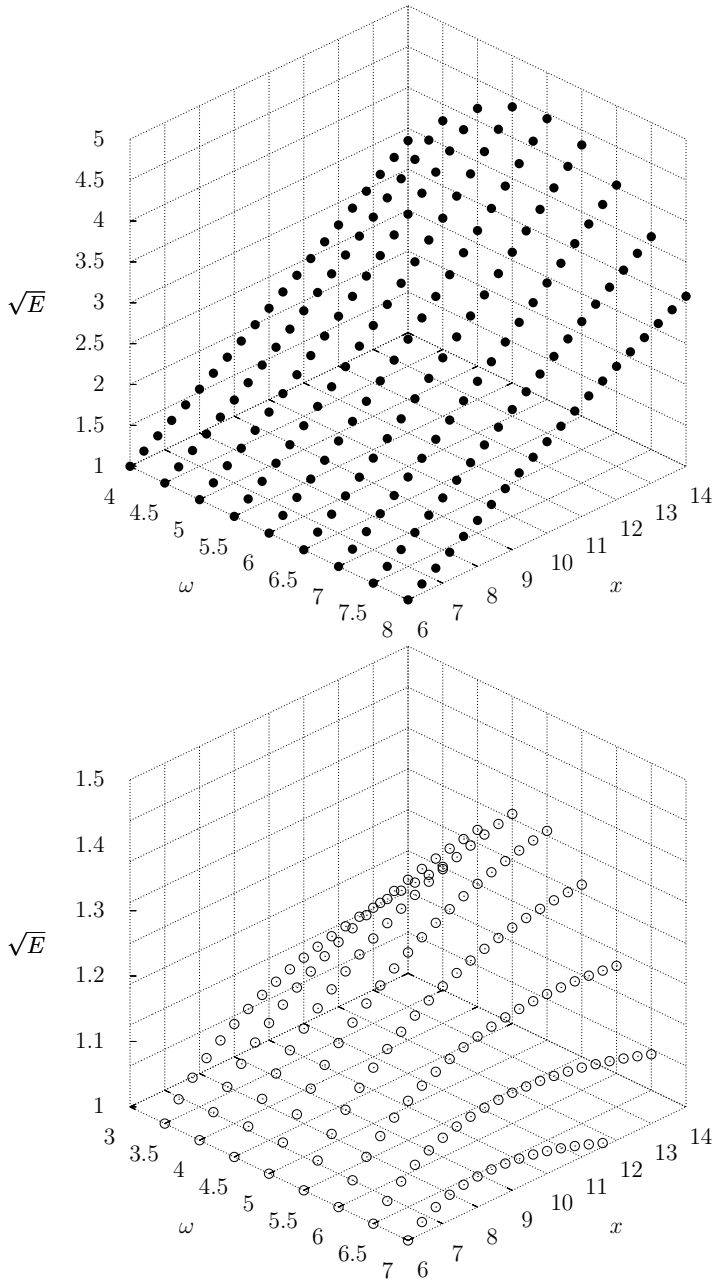

Fig. 9 Kinetic energy of symmetric (upper) and anti-symmetric (lower) perturbations obtained with linear PSE-3D on the AR=1.7 wing as a function of the axial coordinate x for a range of amplified frequencies ω

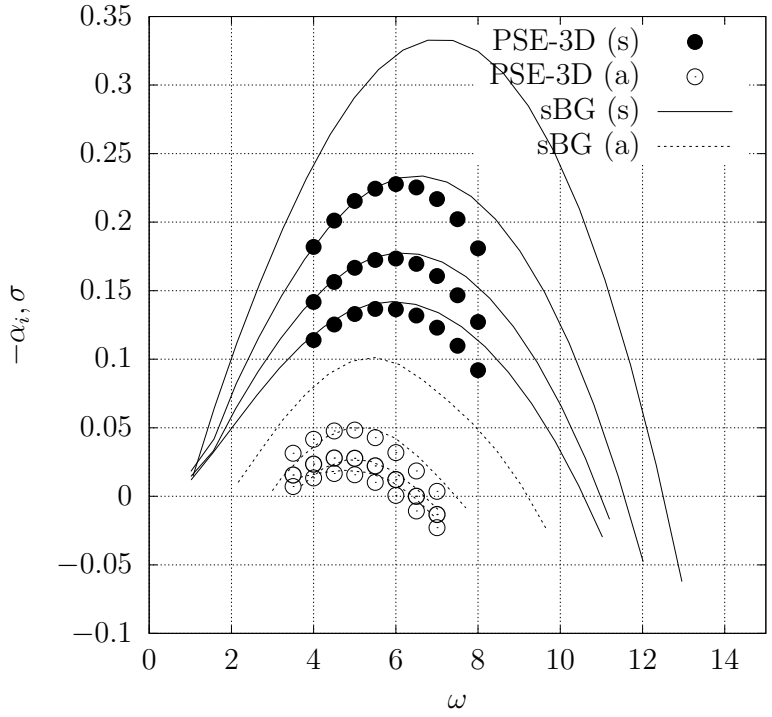

Fig. 10 Dependence on the frequency ω of spatial amplification rates, $-\alpha_i$ (spatial BiGlobal EVP – lines) and σ (PSE-3D – symbols), for both symmetric (s) and antisymmetric (a) boundary conditions. Upper to lower curves correspond to the locations $x = 6, 8, 10$ and 12 in both sets of results. PSE-3D computations have been initialized with results at $x = 6$

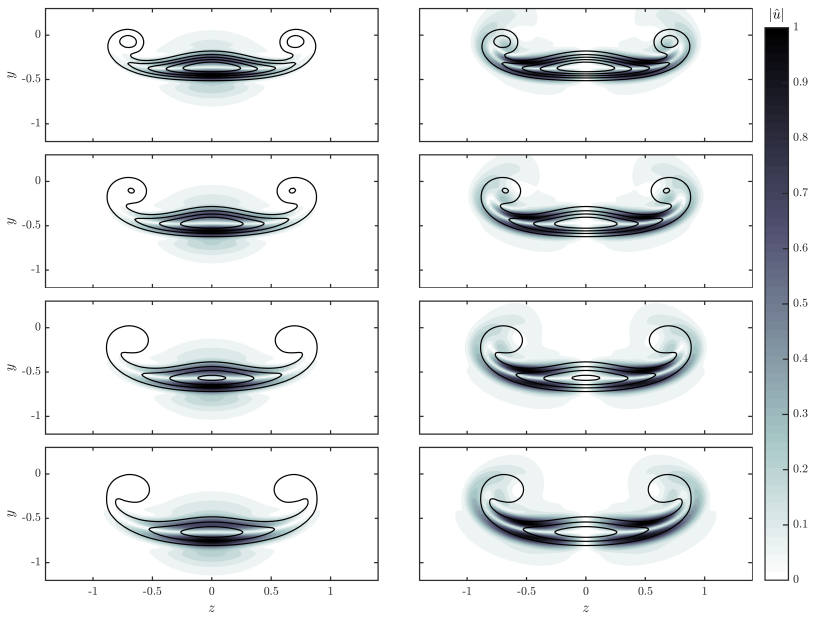

Fig. 11 Evolution of the amplitude functions $\hat{u}_1(y, z)$ with axial distance. *Upper to lower*: $x = 6, 8, 10$ and 12. *Left column*: symmetric perturbations at $\omega = 6$. *Right column*: antisymmetric perturbations at $\omega = 5$

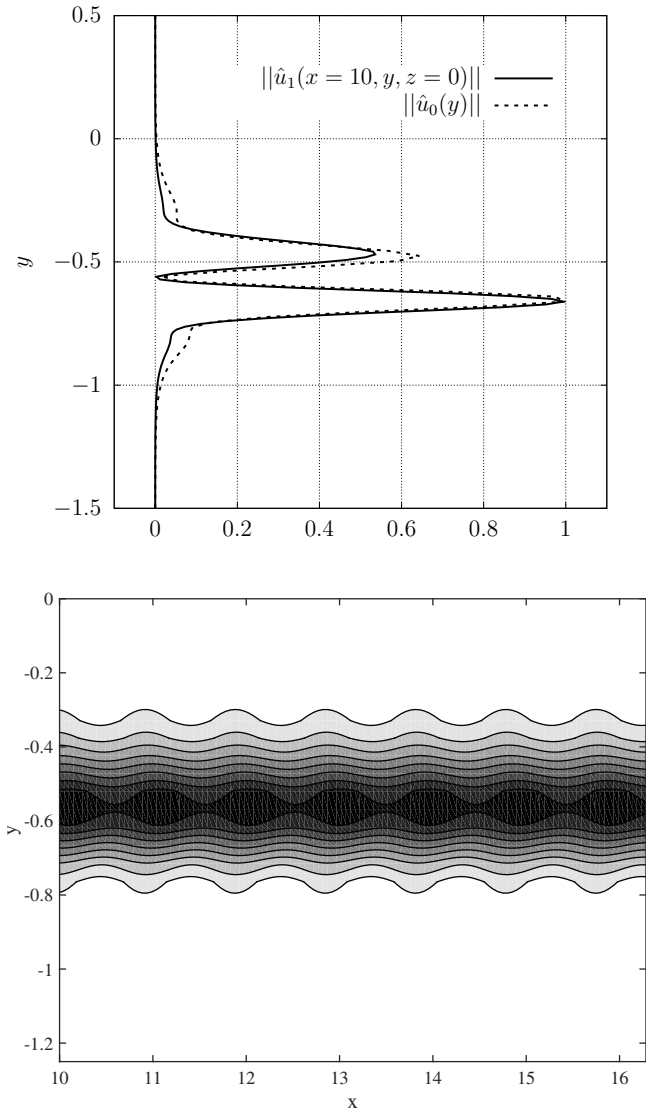

Fig. 12 *Upper:* Comparison of the amplitude function $\hat{u}_0(y)$ of the leading eigenmodes delivered by the Orr-Sommerfeld equation at $x = 10$ with the profile extracted from the the leading two-dimensional eigenfunction $\hat{u}_1(x = 10, y, z = 0)$ obtained by solution of (10). *Lower:* Instability in the wake, predicted by local analysis.

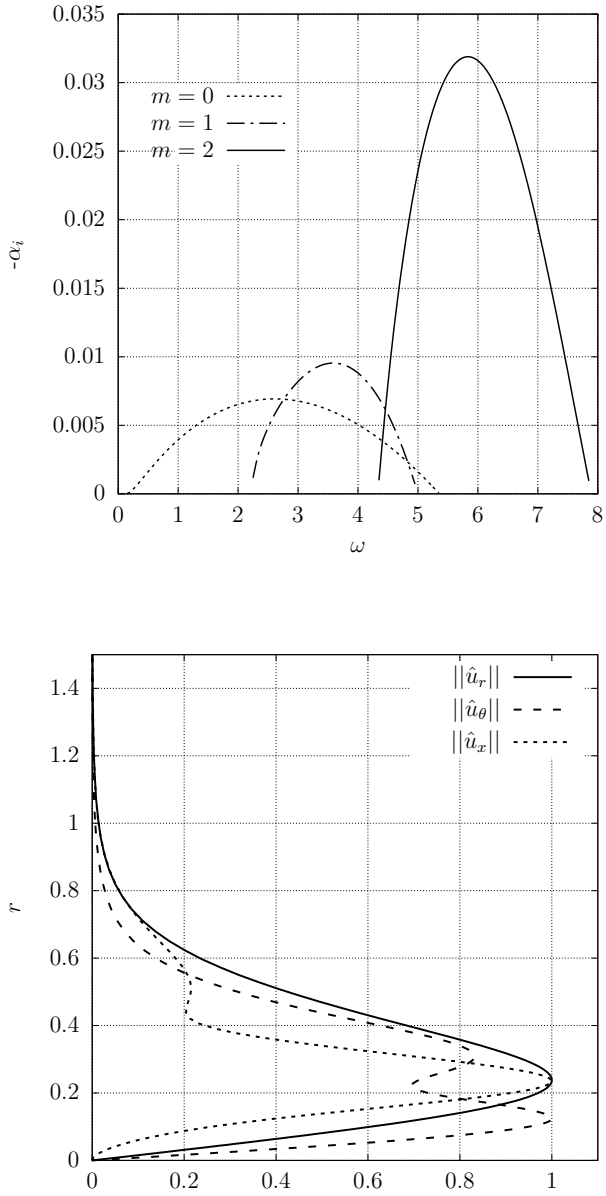

Fig. 13 *Upper:* Leading eigenmodes of local analysis in the neighborhood of the vortex. *Lower:* Amplitude functions of the leading $m = 2$ eigenmode around the vortex core at $x = 10, \omega = 5.85$; $r = \left[(y - y_c)^2 + (z - z_c)^2\right]^{\frac{1}{2}}$

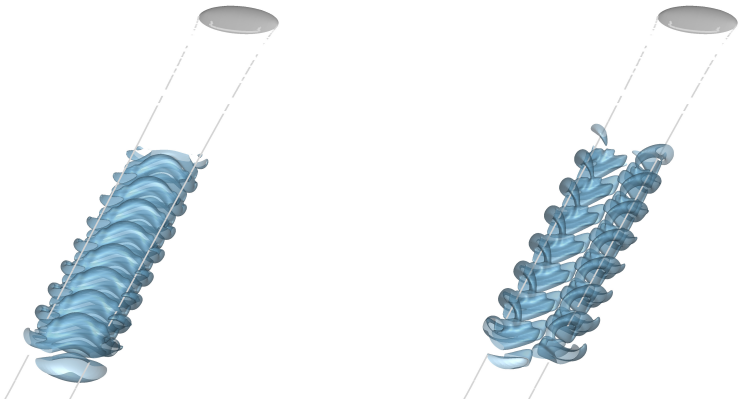

Fig. 14 Perspective view of isosurfaces of streamwise perturbation velocity of symmetric (*left*) and anti-symmetric (*right*) disturbances obtained by linear PSE-3D analysis, superposed upon the image of base flow vortex core positions